

# The final verdict by XMM-Newton: the X-ray obscured Seyfert galaxy NGC 5506 has a broad Fe $K_\alpha$ line

M. Guainazzi<sup>\*</sup>,<sup>1</sup> S. Bianchi,<sup>2</sup> G. Matt,<sup>2</sup> M. Dadina,<sup>3</sup> J. Kaastra,<sup>4</sup> J. Malzac,<sup>5</sup> G. Risaliti,<sup>6,7</sup>

<sup>1</sup>European Space Astronomy Center of ESA, P.O.Box 78, Villanueva de la Cañada, E-28691 Madrid, Spain

<sup>2</sup>Dipartimento di Fisica, Università degli Studi Roma Tre, via della Vasca Navale 84, I-00046 Roma, Italy

<sup>3</sup>INAF/IASF-Bo, via Gobetti 101, I-40129 Bologna, Italy

<sup>4</sup>SRON Netherlands Institute for Space Research, Sorbonnelaan 2, 3584 CA Utrecht, The Netherlands

<sup>5</sup>Centre d'Etude Spatiale des Rayonnements, Université de Toulouse, CNRS, 9 avenue du Colonel Roche, BP 44346, 31028 Toulouse Cedex 4, France

<sup>6</sup>Harvard-Smithsonian Center for Astrophysics, 60 Garden St. Cambridge, MA 02138, USA

<sup>7</sup>INAF-Osservatorio di Arcetri, Largo E. Fermi 5, I-50125, Firenze, Italy

## ABSTRACT

We present the first unambiguous evidence of a broad (Gaussian width  $\sim 330$  eV) component of the iron  $K_\alpha$  fluorescent emission line in the X-ray obscured Narrow Line Seyfert 1 Galaxy NGC 5506. This is the main results of a spectroscopic monitoring campaign on this source performed with the XMM-Newton observatory between February 2001 and January 2009. The broad line lacks extreme redwards skewness. If modelled with a relativistic component, the profile of the line is consistent with a flat emissivity radial dependence ( $\alpha \simeq 1.9$ ). The disk inclination ( $\simeq 40^\circ$ ) is nominally larger than typically observed in unobscured AGN, in agreement with most measurements of broadened iron lines in Seyfert 2 galaxies. The quality of the data allows us to decompose the full iron emission line complex, and to study its long-term (timescales of weeks to years) variability pattern. The intensity of the neutral and narrow iron  $K_\alpha$  core remains constant during the monitoring campaign. This indicates that the optically thick gas responsible for the non-relativistic reprocessing of the primary AGN continuum in NGC 5506 is probably located in the torus rather than in the optical Broad Line Region.

**Key words:** Galaxies: active – Galaxies:Seyferts – X-rays:galaxies – X-rays:individual:NGC 5506

## 1 INTRODUCTION

Broadening by relativistic effects of emission lines in an X-ray illuminated accretion disk offers the opportunity of probing the physical conditions and geometrical distribution of matter in the vicinity of black holes, as well as General Relativity effects (Reynolds & Nowak 2003; Miller 2007). Broad and skewed profiles of the iron  $K_\alpha$  fluorescent emission line were discovered by ASCA in the mid-90s (Tanaka et al. 1995; Mushotzky et al. 1995). High-throughput observations with the EPIC cameras on-board XMM-Newton have shown that at least 30 percent of nearby Seyfert galaxies exhibit relativistically blurred features consistent with being produced within 50 gravitational radii ( $r_g \equiv GM/c^2$ , where  $M$  is the black hole mass) (Nandra et al. 2007). However, doubts have been cast on

the robustness and uniqueness of these results. Ionised outflows partially covering the primary high-energy emission in AGN could mimic relativistic effects (Turner & Miller 2009; Reeves et al. 2004). Controversy is fierce. In this context, it is crucial to confirm whether objects, whose data had poor signal-to-noise, do exhibit relativistically broadened lines as well as to expand the parameter space covered by these measurements.

The study of X-ray obscured AGN is particularly promising. In the “Unified Model” framework (Antonucci & Miller 1985; Antonucci 1993), their putative accretion disks are expected to be observed at higher inclination angles if the plane of the disk is aligned with that of the obscuring matter. For inclinations not too close to “edge-on”, special relativistic effects, such as Doppler boosting, should be therefore stronger and easier to detect. Moreover, in type II objects the polar outflows should be out of the line of sight and this should break the de-

\* E-mail:Matteo.Guainazzi@sciops.esa.int

generacy between "warm absorbers" and relativistic lines (Turner & Miller 2009). Finally relativistic lines allow the direct measurements of the inclination angle of the accretion disk thus offering a simple test of the unified scenarios.

Observations of broad Fe line in X-ray obscured Seyferts are so far sparse. The Fe  $K_\alpha$  line in the *Suzaku* spectrum of MCG-5-23-16 implies a disk inclination,  $i$ , of  $53^\circ \pm 7^\circ$  (Reeves et al. 2007)<sup>1</sup>. Nandra et al. (2007) add to this census NGC 526A ( $i=43^\circ \pm 20^\circ$ ) and NGC 2992 ( $i=24^\circ \pm 7^\circ$ ), whereas NGC 2110 and Mkn 6 do not exhibit significant evidence for relativistic effects. NGC 1365 ( $i=24^\circ \pm 8^\circ$ ; Risaliti et al. 2009) and IRAS13197-1627 ( $i=27^\circ \pm 17^\circ$ ; Dadina & Cappi 2004, Miniutti et al. 2007b) were also recently discovered to host broad lines from nominally low inclination disks. The aforementioned uncertainties are purely statistics; systematic uncertainties related *e.g.* to different spectral deconvolutions are seldom discussed in the literature. They can be at least comparable to the statistical ones.

In this context, the case of the nearby ( $z = 0.0061$ ) X-ray obscured ( $N_H \simeq 3 \times 10^{22} \text{ cm}^{-2}$ ; Wang et al. 1999) Narrow Line Seyfert 1 Galaxy (NLSy1; Nagar et al. 2002) NGC 5506 is one of the most controversial. Bianchi et al. (2003) analysed all the X-ray observations performed with imaging and spectroscopic instruments on NGC 5506 at that time. They did not detect any spectral components directly related to the accretion disk. This led them to conclude that the disk is either fully ionised, or almost edge-on. Two early XMM-Newton observations of NGC 5506 (originally presented by Matt et al. 2001) are also in the Nandra et al. (2007) sample. In their analysis, only one observation shows evidence of broadened emission. Nandra et al. (2007) interpreted the lack of detection as simply due to low signal-to-noise ratio.

In this paper we present spectroscopic results of a XMM-Newton monitoring campaign of NGC 5506, which brings the total integration time to  $\simeq 197$  ks (versus the 23 ks of the observations published so far). The main results of this paper is the *first unambiguous detection of a broad iron  $K_\alpha$  line in NGC 5506*.

## 2 OBSERVATIONS AND DATA REDUCTIONS

Tab. 1 lists the XMM-Newton observations of NGC 5506 performed so far. We discuss in this paper data of the EPIC cameras only (MOS, Turner et al. 2001; pn, Strüder et al. 2001). Data were reduced using the SASv9.0 (Gabriel et al. 2003) tasks `e[mp]proc` with standard settings. Periods of high-background were removed using count rate thresholds on the high-energy, single events, field-of-view light curves (Tab. 1) which optimise the signal-to-noise of each individual observation. Source spectra were extracted from circular regions surrounding the source centroid (Tab. 1), whereas background spectra from circular regions on the same chip free from contaminating serendipitous sources (and at the same height in detector coordinates for the pn to ensure that the same Charge Transfer Inefficiency correction applies). Response files were generated with the SAS tasks `arfgen` and `rmfgen`. Spectra were

<sup>1</sup> see, however, Nandra et al. (2007), whose spectral deconvolution of the XMM-Newton/EPIC spectra requires  $i \lesssim 20^\circ$

**Table 1.** Log of XMM-Newton NGC 5506 observations

XMM-N ID	Start Time	$\rho^a$ ( $''$ )	$T_{CR}^b$ ( $\text{s}^{-1}$ )	$T_{exp}^c$ (ks)
0013140101 (1) <sup>d</sup>	02-02-2001	100/40	0.2/0.5	13.3
0013140201 (2) <sup>d</sup>	09-01-2002	120/44	0.5/1.0	9.9
0201830201 (3) <sup>d</sup>	11-07-2004	42/45	0.5/0.5	14.8
0201830301 (4) <sup>d</sup>	14-07-2004	40/42	0.5/0.35	13.9
0201830401 (5) <sup>d</sup>	22-07-2004	40/42	0.35/0.35	13.8
0201830501 (6) <sup>d</sup>	07-08-2004	40/42	0.35/0.35	13.9
0554170101 (7) <sup>d</sup>	27-07-2008	50/50	0.35/0.35	55.8
0554170201 (8) <sup>d</sup>	02-01-2009	40/40	0.5/0.35	62.0

<sup>a</sup>size of the source spectrum extraction region in the MOS/pn; <sup>b</sup>count rate threshold applied to select intervals of low particle background in the MOS/pn; <sup>c</sup>pn exposure time; <sup>d</sup>label used to identify the observation in this paper: XMM*i*

rebinned to over-sample the intrinsic energy resolution by a factor not larger than 3, and to ensure that each spectral channel has a number of background-subtracted counts larger than 50. Spectral fits were performed in the 2.2–10 keV energy band, to avoid large gradients of the instrument transfer function due to the instrumental edges (1.8–2.2 keV) and to the soft X-ray photoelectric cut-off. Below the energy of the latter the X-ray spectrum is dominated by reprocessing and scattering of the nuclear radiation by photoionised gas on scales as large as a few hundreds parsecs (Bianchi et al. 2003). High-resolution spectroscopy of this component will be discussed elsewhere (Labiano et al., in preparation).

In this paper: energies are quoted in the source rest frame; errors are quoted at the 90% confidence level for one interesting parameter; the following cosmological parameters have been adopted in the calculation of the luminosities:  $H_0=70 \text{ km s}^{-1} \text{ Mpc}^{-1}$ ,  $\Lambda_0=0.73$ ,  $\Omega_m=0.27$  (Bennett et al. 2003).

## 3 SPECTRAL ANALYSIS

### 3.1 Phenomenological fits on individual observations

As first step, we fit the pn spectrum of each individual XMM-Newton observation with the same phenomenological model. Following the approach as in Matt et al. (2001), the model is constituted by a photoelectrically absorbed power-law, a photoelectric absorption edge and three narrow iron emission lines, modelling the  $K_\alpha$  fluorescence of Fe I and of recombination lines of FeXXV and FeXXVI. The Fe I and FeXXVI are actually each close doublets, which cannot be resolved by the EPIC cameras. Their centroid energy has been fixed to the weighed mean of the corresponding doublet components: 6.399 keV and 6.966 keV, respectively. The structure of the FeXXV line is instead more complex, with the resonance (6.7002 keV), two intercombination (6.6821 keV, and 6.6673 keV) and the forbidden components (6.6364 keV) all potentially contributing. In the fit of each observation we left originally the FeXXV centroid energy free to vary. We obtained lower limits consistent with the energy of the resonance line (and inconsistent with the other components) in all observations, except in XMM8, where

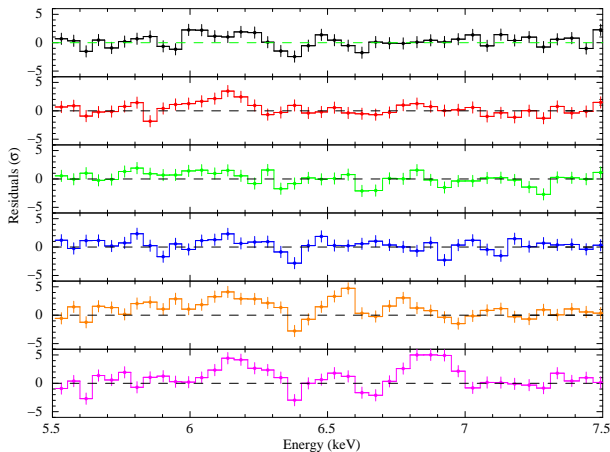


**Figure 1.** 5.5–7.5 keV residuals in units of standard deviations when the best-fit phenomenological model is applied to the 2.2–12 keV EPIC-pn spectra of the 2004–2009 XMM-Newton observations of NGC 5506.

$E_c^{FeXXV} = 6.654 \pm_{0.017}^{0.020}$  keV [ $I = (3.7 \pm 1.0) \times 10^{-5}$  photons  $\text{cm}^{-2} \text{s}^{-1}$ ]. In all the subsequent models we fixed the centroid energy of the FeXXV line to the value of the resonance component, except for XMM8 for which we used the value of the forbidden component. Finally, the energy of the edge was constrained to be  $\gtrsim 7.11$  keV, corresponding to photoionisation of iron.

The FeI line  $1\text{-}\sigma$  width (only “width” hereafter) is  $46 \pm_{14}^{11}$  eV. This measurement is consistent with the width of the Manganese  $K_\alpha$  and  $K_\beta$  pn calibration emission lines measured in observations close to the 2009 NGC 5506 observations:  $\sigma_{cal} = 42 \pm 8$  eV, and  $\sigma_{cal} = 47 \pm 8$  eV in Obs.#0410780601 (August 9, 2008) and Obs.#0412580401 (January 4, 2009), respectively. The measurement is thus consistent with the instrumental resolution. We have consequently used this value for all the nominally unresolved astrophysical emission lines in the models discussed in this paper.

In Fig. 1 we show the residuals against the best-fit phenomenological model in the 5.5–7.5 keV energy band (the residuals are flat outside this interval). In the longest observations significant wave-like residuals are present around the nominal energy of the FeI fluorescent  $K_\alpha$  line. Hints of features with a similar shape are visible in other observations with a lower statistics. These features can be interpreted as being due to a broad ( $\sigma \simeq 300$  eV) excess emission feature, which the narrow FeI Gaussian profile is unable to account for.

In Fig. 1 we do not show the residuals for the first two observations (XMM1 and XMM2). The event pattern distribution measured by the SAS task `epatplot` suggests that they might be marginally affected by pile-up due to the different instrument mode (Large Window instead of Small Window). This may also explain why XMM2 - which corresponds to the highest X-ray flux measured during our campaign - exhibits the flattest X-ray spectral index. This is illustrated in Fig. 2, where the best-fit parameters of the phenomenological model in each individual fit as a function of time and of the 7–12 keV absorption-corrected flux are shown, once the excess emission around 6 keV is fit with a further Gaussian profile whose width was left free to vary.

The intensity of the narrow FeI line is constant. Its mean normalised dynamical range is  $\leq 27\%$ . Evidence for variability of the recombination He- and H-like line intensity is also marginal. Beside the possible change of ionisation state of the FeXXV in XMM8, it is limited to a nominal difference by a factor of at least five between two measurements of the FeXXVI line during the 2004 monitoring campaign. Given the uncertainties in the spectral deconvolution at  $\simeq 7$  keV, we consider this evidence for variability as only tentative, to be confirmed by high-resolution measurements.

We have applied the same phenomenological model also to the combined spectra extracted from the MOS cameras. The parameters of the continuum are different. The ratio between the 2–10 keV MOS and pn fluxes (weighted mean,  $\langle F_{MOS}/F_{pn} \rangle = 5.5\%$ ;  $\sigma_{F_{MOS}/F_{pn}} = 2.7\%$ ) is consistent with known systematic calibration uncertainties in the absolute flux determination (Stuhlinger et al. 2008). However, the average difference between the spectral index ( $\langle \Delta\Gamma \rangle = 0.23$ ;  $\sigma_{\Delta\Gamma} = 0.07$ ) and the column density ( $\langle \Delta N_H \rangle = 4.9 \times 10^{21} \text{ cm}^{-2}$ ;  $\sigma_{\Delta N_H} = 2.0 \times 10^{21} \text{ cm}^{-2}$ ) is larger than expected. The difference is larger for higher fluxes. The continuum spectral parameters measured by the EPIC cameras are instead well consistent for observations whose 2–10 keV flux is lower than  $\simeq 8 \times 10^{-11} \text{ erg cm}^{-2} \text{ s}^{-1}$ . Visual inspection of the MOS pattern fraction distribution unveiled an excess (deficit) of double (single) events by 15–30% above 4 keV in higher flux observations. The above pieces of evidence indicate that many of the NGC 5506 MOS spectra could be still affected by pile-up. Consequently, we will not discuss the MOS spectra in the rest of the paper. However, we will show in Sect. 3.2 that the main result of this paper - the ultimate discovery of a broad component of the iron  $K_\alpha$  line - is measured in *both* the pn and the MOS cameras with comparable properties.

## 3.2 Physically-motivated combined fits of all observation spectra

### 3.2.1 Description of the models

Motivated by the results presented in the previous Section, we enriched the phenomenological model by adding physically-motivated components to account for features detected in the spectral residuals. We have investigated three main scenarios:

- Scenario #1: relativistically broadened  $K_\alpha$  iron line and non-relativistic Compton reflection. The former component has been modelled through the code `kyrline` (Dovčiak et al. 2004), which calculates the profile of an emission line produced in an axisymmetric accretion disk around a black hole. The Compton-reflection component (model `pexrav`; Magdziarz & Zdziarski 1995) is primarily associated in this scenario to the narrow core of the iron  $K_\alpha$  line, although it may include a contribution by the accretion disk as well, which the moderate energy resolution of the EPIC cameras is unable to disentangle.
- Scenario #2: non-relativistically broadened  $K_\alpha$  iron line and Compton reflection. The former component has been modelled with a simple Gaussian profile
- Scenario #3: relativistically broadened emission line and continuum reflection dominated by a relativistically

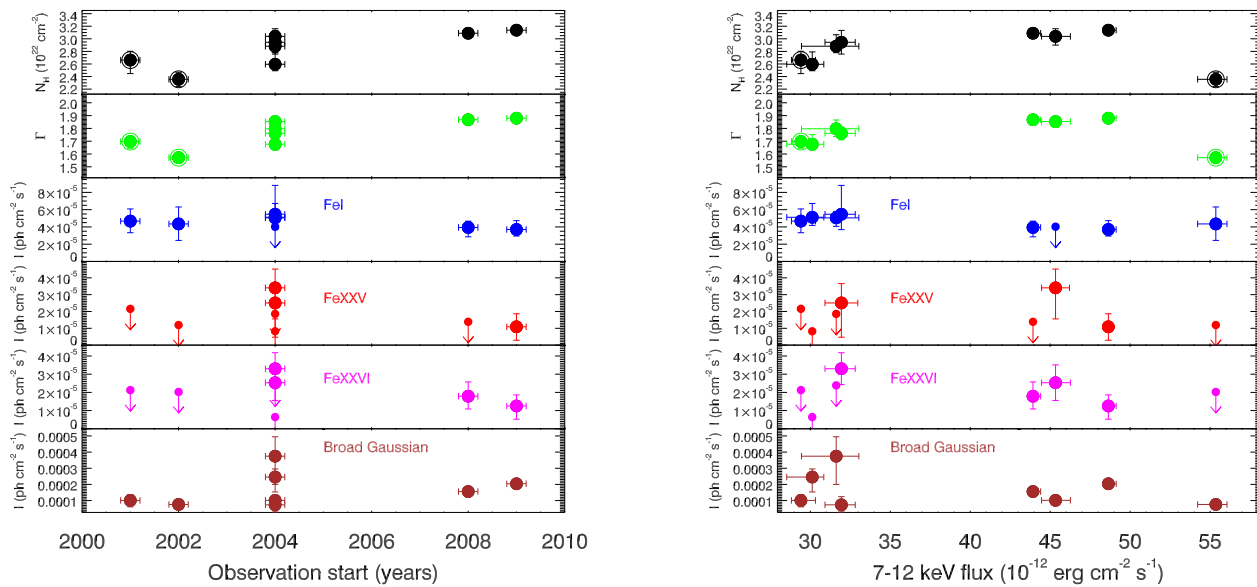


**Figure 2.** Best-fit parameters of the phenomenological fits of individual NGC 5506 XMM-Newton observations as a function of time (*left panel*) and of the 7–12 keV absorption-corrected flux (*right panel*): from *top to bottom*: photon index, column density, intensity of the FeI, FeXXV, FeXXVI narrow emission lines and of the broad Gaussian. Continuum measurement data points corresponding to pn observations in Large Window mode are surrounded by a *large circle*.

blurred component. The latter component has been modelled by convolving `pexrav` with the relativistic kernel `kyconv` (Dovčiak et al. 2004) and assuming a constant ratio between the normalisation of the primary continuum and that of the Compton reflection ( $R$ , see Tab. 2).

`kyrline` belongs to a suite of models based on a common ray-tracing subroutine aiming at describing the X-ray emission of black-hole accretion disks in the strong gravity regime (Dovčiak et al. 2004). The line profile depends on the following parameters: a) the black hole spin  $a$  (comprised between 0 and 0.9982 in dimensionless relativistic units); b) the inner ( $r_{in}$ ) and outer ( $r_{out}$ ) radius of an annular region on the disk where the line photons are emitted; c) the index  $\alpha$  of the radial dependence of the emissivity per unit area,  $\kappa$ , in the local frame comoving with the disk:  $\kappa(r) \propto r^{-\alpha}$ ; d) the “disk inclination”  $i$ , i.e. the angle between the normal to the disk plane and the line-of-sight; e) the rest frame energy (assumed monochromatic) of the photons emitted by the disk,  $E_c$ . Although the line normalisation in `kyrline` is expressed in units of photons  $\text{cm}^{-2} \text{s}^{-1}$  integrated over the whole profile, we will also use the line Equivalent Width (EW), i.e. the line intensity normalised to the underlying continuum at 6.4 keV, to ease comparison against theoretical predictions (Matt et al. 1992). The convolution function `kyconv` uses the same relativistic kernel as `kyrline`.

The continuum reflection components replace the photo-absorption edge in the phenomenological model. We always linked together the spectral index of the Compton-reflected continuum and that of the primary emission. Moreover, we have added two narrow-band spectral components to the non-relativistic emission line complex, modelling the: a) iron  $K_\alpha$  fluorescent iron line Compton-shoulder (Sunyaev & Churazov 1996; Matt 2002) through a rectan-

gular box function comprised between 6.24 and 6.4 keV, and whose intensity was constrained to be not larger than 20% the intensity of the corresponding narrow  $K_\alpha$  line (the fits determine only an upper limit on this parameter as large as the maximum allowed value); b) the  $K_\beta$  line associated with the iron  $K_\alpha$  narrow component, modelled with a Gaussian profile with energy fixed at 7.058 keV and intensity constrained not to exceed 16% of the  $K_\alpha$  intensity (Molendi et al. 2003).

In principle, only model parameters describing physical quantities not expected to change among the observations (or demonstrated to remain constant in the phenomenological analysis) have been constrained to have the same value for all fitted spectra. They are: the intensities of the narrow FeI, FeXXV and FeXXVI lines; the metallicity (assumed solar; Anders & Grevesse 1989); the high-energy cut-off of the intrinsic primary continuum (held fixed to 130 keV in accordance to the results of the BeppoSAX observation; Bianchi et al. 2003); the inclination of the disk and of the distant non-relativistic reflector (the latter held fixed to  $45^\circ$ ); and the black hole spin. In Scenario #1 and #3 varying the black hole spin from Schwarzschild to maximally rotating yields a variation of the  $\chi^2$  lower than 0.5. We have therefore fixed this parameter to the value corresponding to the latter solution ( $a = 0.998$ ), favoured at face value. Once these assumptions were made, a first series of fits showed that many of the remaining free parameters were consistent with being constant across all the fitted observations. We have therefore forced them to assume the same value in all the fits. In Scenarios #1 and #3 they are: a) the inner and outer radius of the X-ray emitting disk. Initially we have fixed the latter to  $400r_g$ , because this parameter is generally unconstrained when the line profile is strongly relativistic. We will

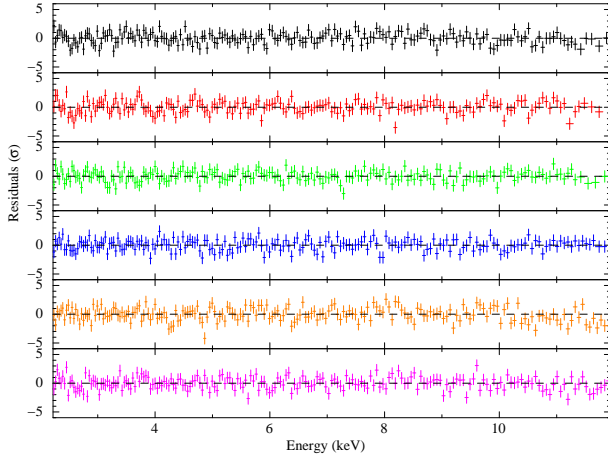


**Figure 3.** Residuals in units of standard deviation when the Scenario#3 best-fit model is applied to the 2004-2009 EPIC-pn spectra. From *top to bottom*: XMM3, XMM4, XMM5, XMM6, XMM7, XMM8. Y-axis range and colours are the same as in Fig. 1

review this assumption in Sect. 3.2.2. The former has been constrained throughout the paper to coincide with the innermost stable circular orbit of an accretion disk co-rotating with a black hole of spin  $a$ ; b) the index of the power-law disk emissivity radial dependence,  $\alpha$ ; c) the energy of the relativistically broadened line in the source rest frame,  $E_c$ . In Scenario #2 they are all the parameters describing the broad Gaussian profile.

### 3.2.2 Results

The Scenarios described above yield comparable fit qualities:  $\chi^2/\nu=1265.3/1161$ ,  $1280.9/1161$ , and  $1258.1/1161$  for Scenario #1, #2, and #3, respectively. These  $\chi^2$  are significantly better than those yielded by the same models *without* the broad line:  $1479.5/1169$ ,  $1516.2/1169$ , and  $1581.6/1166$ , respectively. No further structure is visible in the residuals (Fig. 3). We therefore concluded that no additional astrophysical component is required. In Tab. 2 we summarise the best-fit results for the non-relativistic components in Scenario#3. The values for the other scenarios are consistent with them within the statistical uncertainties. In Fig. 4 we show the spectra of observations XMM3 to XMM8 together with the components of their best-fit models.

The properties of the relativistic line can be summarised as follows (see Tab. 3): a) the rest frame centroid energy is consistent with neutral or moderately ionised iron ( $E_c \simeq 6.48$  keV). Fixing the source frame centroid energy to the value expected for neutral iron in, *e.g.*, Scenario#3 yields  $\chi^2 = 1276.0/1160$  dof; b) the disk is slightly more inclined ( $i \simeq 40^\circ$ ) than typically measured in unobscured Seyfert galaxies (Nandra et al. 1997; Nandra et al. 2007), and; c) the line profile is only mildly relativistic as parametrised by the moderately flat ( $\alpha \simeq 1.9$ ) radial emissivity profile. The line emitting region extends close to the innermost stable orbit. The innermost radius is constrained between 3 and  $25 r_g$ . In Fig. 5 we show the profile of the relativistically broadened iron line, obtained by stacking together the source frame residuals of each individual observation against the best-fit model in Scenario#3 once the relativistically

**Table 2.** Best-fit results for the parameters of the non-relativistic continuum components in Scenario #3 (except parameter  $EW_{FeI}$  which refers to Scenario#1).

Spectrum dependent parameters			
Obs.#	$N_H$ ( $10^{22} \text{ cm}^{-2}$ )	$\Gamma$	2–10 keV Flux <sup>a</sup> ( $10^{-12} \text{ erg s}^{-1} \text{ cm}^{-2}$ )
XMM3	$2.86 \pm 0.11$	$1.778 \pm 0.014$	$82.5 \pm 0.6$
XMM4	$2.94 \pm 0.12$	$1.777 \pm 0.013$	$79.4 \pm 1.2$
XMM5	$2.65 \pm 0.12$	$1.771 \pm 0.014$	$71.4 \pm 0.7$
XMM6	$2.99 \pm 0.12$	$1.844 \pm 0.015$	$120.0 \pm 0.6$
XMM7	$3.08 \pm 0.04$	$1.864 \pm 0.009$	$132.5 \pm 1.3$
XMM8	$3.04 \pm 0.06$	$1.862 \pm 0.010$	$118.7 \pm 0.9$

### Spectrum independent parameters

$$J_{FeI}^b = (5.9 \pm 0.6) \times 10^{-5} \text{ erg cm}^{-2} \text{ s}^{-1}$$

$$J_{FeXXVr}^b \leq 1.0 \times 10^{-5} \text{ erg cm}^{-2} \text{ s}^{-1}$$

$$J_{FeXXVf}^b \leq 1.4 \times 10^{-5} \text{ erg cm}^{-2} \text{ s}^{-1}$$

$$J_{FeXXVI}^b = (2.0 \pm 0.7) \times 10^{-5} \text{ erg cm}^{-2} \text{ s}^{-1}$$

$$R \leq 0.1^c$$

$$EW_{FeI} \geq 1.0 \text{ keV}^d$$

<sup>a</sup>corrected for absorption. XMM1:  $70.8 \pm 1.0$ ; XMM2:  $121.1 \pm 1.4$  in the same units; <sup>b</sup>intensity of the narrow emission lines; <sup>c</sup>ratio between the primary continuum and the relativistically blurred reflection normalisation; <sup>d</sup>Equivalent Width of the narrow component of the FeI fluorescent line against its own reflection continuum.

**Table 3.** Best-fit values of the  $K_{\alpha}$  iron relativistically broadened profile in Scenarios #1 and #3 for  $r_{out}=400r_g$ . The *rightmost column* contains the statistical uncertainties to be added if  $r_{out}$  is allowed to vary.

	Scenario #1	Scenario #3	Additional error if $r_{out}$ is left free
$E_c$ (keV)	$6.48 \pm 0.02$	$6.48 \pm 0.02$	$\pm 0.02$ $\pm 0.00$
$\alpha$	$1.9 \pm 0.3$	$1.9 \pm 0.3$	$\pm 0.1$
$i^\circ$	$42 \pm 6$	$37 \pm 5$	$\pm 11$ $\pm 4$
$r_{in}$ ( $r_g$ )	$15 \pm 9$	$15 \pm 9$	$\pm 7$ $\pm 1$

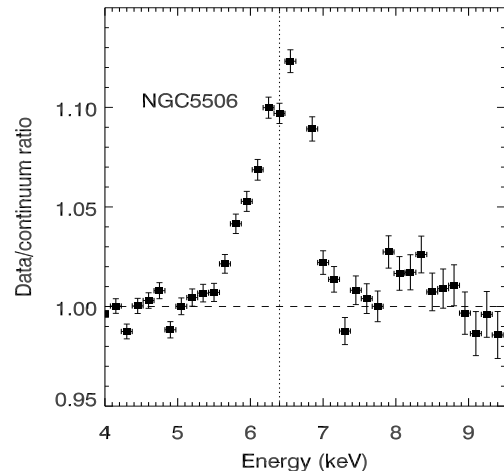


**Figure 5.** Stacked profile of the relativistically broadened iron line. The *dashed line* indicates the observed frame energy of the neutral iron  $K_{\alpha}$  fluorescent line.

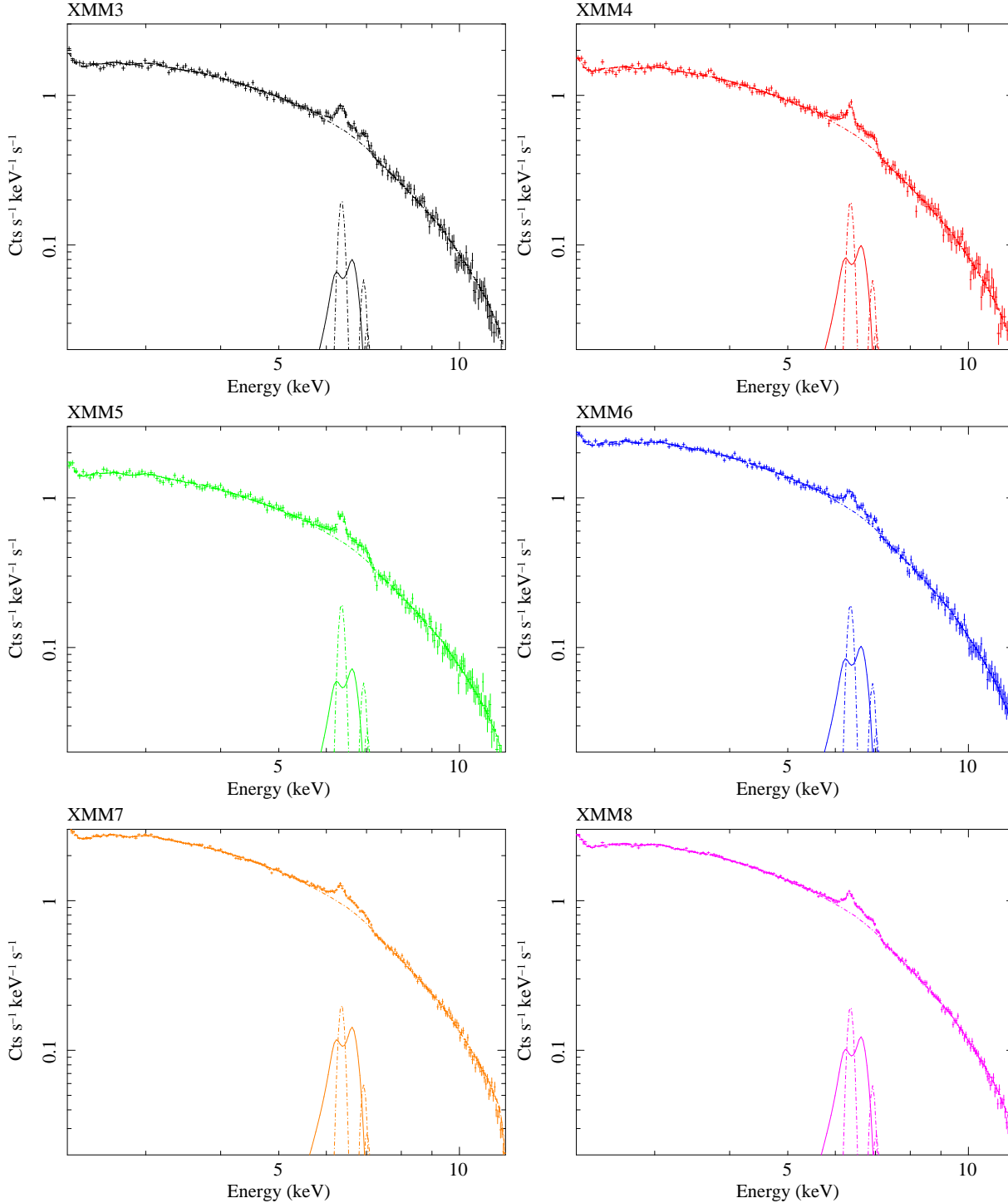


**Figure 4.** EPIC-pn NGC 5506 spectra in observations XMM3 to XMM8 (*crosses*). The *lines* indicate different model components: *dot-dashed*: continuum; *long dot-dashed*: narrow lines; *solid*: broad line.

broadened emission line had is removed from the model. The profile is not significantly skewed. This is consistent with the similar fit quality that relativistic and non-relativistic scenarios yield. A small “dip” in the profile coincide exactly with the rest frame energy of the  $K_{\alpha}$  neutral iron fluorescent line. It could be due to an incorrect disentangling between the narrow and the broad profile, whereby the fit preferentially attributes photons in this energy range to the former.

We estimate that the intensity of the narrow component should be lowered by at least 50% for the dip to disappear. The effect of this potential systematic uncertainty on the determination of the relativistic line profiles  $\alpha$  and  $r_{in}$  is negligible, because they are mostly sensitive to the red wing. On the other hand, centroid energy and inclination angle could be affected. Assuming  $I_{FeI} = 3 \times 10^{-5}$  photons  $\text{cm}^{-2} \text{s}^{-1}$ , they change by  $\Delta E_c \simeq 30$  eV and  $\Delta i \simeq 4^{\circ}$ , respectively.



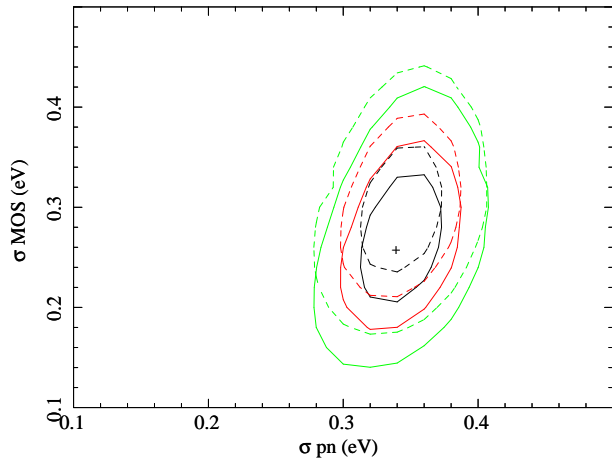


**Figure 6.** Iso- $\chi^2$  contour plots for the intrinsic width of a Gaussian profile fitting the broad component of the iron  $K_\alpha$  line in the NGC 5506 merged spectra. The contours correspond to the 68%, 90% and 99% confidence level for two interesting parameters, respectively. *Solid lines:* pn versus MOS1; *dashed lines:* pn versus MOS2.

Nonetheless, the  $\chi^2$  significantly worsens (1361.9/1160 dof in Scenario#3). This hypothesis is then inconsistent with the data.

We come back now to the original restriction imposed to the value of  $r_{out}$ . The flat value of  $\alpha$  implies that a not negligible contribution to the broad line profile comes also from large disk radii. We have therefore repeated the fits in Scenario#3 after allowing  $r_{out}$  to be a free parameter. At the 90% confidence level for one interesting parameter  $r_{out}$  is constrained to be comprised between 250 and  $900r_g$ . The best-fit value is still around  $400r_g$ , hence the best-fit values do not change. However the broad line parameters errors are augmented by a small amount (Tab. 3).

In Scenario #2, the centroid energy of the Gaussian profile is consistent with fluorescence from neutral or moderately ionised iron:  $E_c = 6.45 \pm_{0.05}^{0.04}$  keV. The line width is  $\sigma_b = 330 \pm 40$  eV.

We have checked the robustness of the broad iron line profile against possible data reduction and/or undiagnosed calibration problems. A fit with Scenario#2 on a merged pn spectrum with single and double events yields the following best-fit broad Gaussian profile parameters:  $E_c = 6.47 \pm_{0.03}^{0.04}$  keV,  $\sigma_b = 360 \pm_{30}^{40}$  eV, and  $I_b = (1.47 \pm 0.14) \times 10^{-4}$  ph s $^{-1}$  cm $^{-2}$ . They agree within the statistical uncertainties with the best-fit parameters obtained on a merged pn spectrum extracted with single events only:  $E_c = 6.41 \pm 0.04$  keV,  $\sigma_b = 360 \pm_{70}^{50}$  eV, and  $I_b = (1.55 \pm 0.18) \times 10^{-4}$  ph s $^{-1}$  cm $^{-2}$ . More importantly, the width measured by the pn spectrum agrees with that simultaneously measured by the MOS cameras (Fig. 6).

### 3.2.3 Variability

The EW of the broad component of the iron  $K_\alpha$  line is consistent with being constant among the XMM-Newton observations discussed in this paper (Tab. 4). On the other hand, its *intensity* is not constant. A fit on the broad line intensity versus time relation with a constant yields a  $\chi^2/\nu=11.4/5$  (versus 2.1/5 for the EW). This indicates that in the first

**Table 4.** Measurements of the broad iron  $K_\alpha$  line EW (in eV).

Obs.#	Scenario #1	Scenario #2	Scenario #3
XMM3	$130 \pm_{20}^{40}$	$130 \pm 30$	$120 \pm_{20}^{30}$
XMM4	$180 \pm_{40}^{30}$	$160 \pm 30$	$150 \pm_{20}^{30}$
XMM5	$140 \pm 30$	$130 \pm 30$	$120 \pm 30$
XMM6	$122 \pm_{26}^{17}$	$100 \pm_{20}^{30}$	$110 \pm 20$
XMM7	$152 \pm_{12}^{11}$	$137 \pm_{15}^{13}$	$132 \pm_{17}^{13}$
XMM8	$149 \pm_{15}^{18}$	$143 \pm_{16}^{12}$	$131 \pm 15$
XMM78 <sub>1</sub>	$180 \pm_{30}^{20}$	$140 \pm_{20}^{30}$	$160 \pm 20$
XMM78 <sub>2</sub>	$117 \pm_{13}^{26}$	$90 \pm_{20}^{30}$	$100 \pm_{20}^{30}$
XMM78 <sub>3</sub>	$110 \pm_{20}^{30}$	$90 \pm 20$	$101 \pm_{20}^{18}$
XMM78 <sub>4</sub>	$120 \pm 20$	$100 \pm 20$	$109 \pm_{19}^{16}$

approximation the broad line intensity follows the variation of the underlying continuum.

The absorption-corrected 2–10 keV flux measured during the XMM-Newton observations covers a dynamical range  $\simeq 1.9$ . This is less than a factor of two smaller than measured during the 6-years long intense X-ray monitoring with the RXTE/PCA in the same energy band ( $\simeq 3.5$ ; Uttley & McHardy 2005). The longest time difference between two observations, whose continuum flux differs by more than 27% (the upper limit on the percentage fractional variability of the intensity of the iron  $K_\alpha$  fluorescent line narrow component) is  $\simeq 7.92$  years (XMM8 versus XMM1).

The photon index in observations XMM6 to XMM8 (2–10 keV absorption corrected flux,  $F_{2-10} \geq 1.19 \times 10^{-10}$  erg s $^{-1}$  cm $^{-2}$ ) is systematically steeper than in the others (by  $\Delta\Gamma \simeq 0.08-0.10$ ). There is an intrinsic correlation between the power-law spectral index and the column density of a photoelectric absorber covering it as measured by the spectral fitting. Steep spectra invariably correspond to higher obscuration. In order to disentangle the intrinsic driver of the continuum spectral variability we run two Scenario#3 models, where the power-law index or the column density had been constrained to assume alternatively the same value among all spectra. The quality of the fit - albeit worse than when both parameters are allowed to vary - is better in the case when the power-law is allowed to vary:  $\chi^2/\nu = 1276.4$  against 1300.6/1164, suggesting that variations of the intrinsic continuum are the main driver of this long-term continuum spectral variability.

The X-ray light curve of NGC 5506 shows also rapid variability, by a factor  $\simeq 1.7$  over 250 s ( $\Delta L_X \simeq 1.1 \times 10^{42}$  erg s $^{-1}$ ; Dewangan & Griffiths 2005). The variability is achromatic (Fig. 7; McHardy & Czerny 1987). In order to investigate the possible dependence of the broad line parameters upon the overall source flux on such small timescales, we have combined the event lists of the 2009 observations, and extracted four intensity-resolved spectra, corresponding to the following background-subtracted count rate ranges:  $< 2.9$ , 2.9–3.2, 3.2–3.5, and  $> 3.5$  s $^{-1}$ . These ranges were chosen in such a way that the intensity-resolved spectra have approximately the same net background-subtracted counts. These spectra are labelled as XMM78<sub>*j*</sub> in Tab. 4, with  $j=1$  to 4 (in increasing flux order). The corresponding 2–10 keV absorption-corrected fluxes are:  $109.3 \pm_{1.4}^{1.3}$ ,  $124.3 \pm_{1.6}^{1.3}$ ,  $134.6 \pm_{1.8}^{1.3}$ ,  $145.0 \pm_{1.7}^{1.3} \times 10^{-12}$  erg cm $^{-2}$  s $^{-1}$ , respectively. No

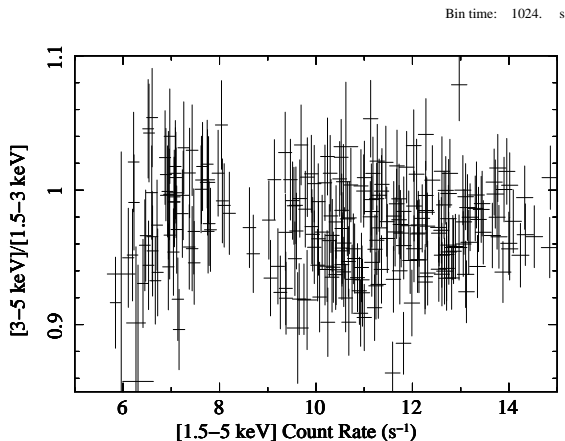


**Figure 7.** 3–5 keV versus 1.5–3 keV hardness ratio as a function of the 1.5–5 keV count rate in all the XMM-Newton observations of Tab. 1.

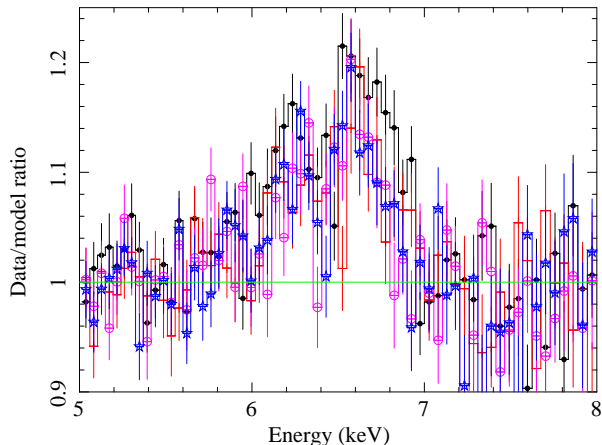


**Figure 8.** Residuals (in units of data/model ratio) when the best-fit continuum in Scenario#3 is applied to intensity-resolved spectra in the nominal energy range excised of the 5–7 keV interval. The contribution of the non-relativistic emission line components was removed as well by subtracting their time-averaged intensity from the residuals. *Filled circles*, XMM78<sub>1</sub>; *crosses*, XMM78<sub>2</sub>; *empty circles*, XMM78<sub>3</sub>; *stars*, XMM78<sub>4</sub>.

correlation exists between the EW of the broad  $K_{\alpha}$  iron line component and the flux (Tab. 4), save for a larger EW in the spectrum corresponding to the lowest flux state. The shape of the broad line component remains also remarkably constant in different flux states (Fig. 8)

## 4 DISCUSSION

### 4.1 Continuum variability

NGC 5506 is one of the most rapidly variable AGN of the X-ray sky. It exhibits luminosity changes of  $\sim 10^{42}$  erg  $s^{-1}$  within a few minutes (Dewangan & Griffiths 2005). The variability is, however, remarkably achromatic on these time scales (Fig. 7; see also McHardy & Czerny 1987). On longer timescales, a small but systematic difference in the intrinsic spectral shape ( $\Delta\Gamma \simeq 0.1$ ) is found between “low flux” and “high flux” observations (absorption-corrected flux ratio be-

tween the latter and the former of about 1.5). An even larger dynamical range in both luminosity and spectral shape was measured during a hard X-rays ( $E > 20$  keV) monitoring campaign with HEXIT (Manchanda 2006). The variability pattern measured by XMM-Newton is inconsistent with a pair-dominated corona (Haardt et al. 1997), where an increase of the spectral index by the amount observed by XMM-Newton requires at least an order-of-magnitude increase of the 2–10 keV luminosity. This does not automatically imply that pairs are not an important source of scattering in the Comptonizing material; the alternative possibility is that the increase of the corona optical depth is due to a variation of the linear dimension of the corona. However, the shape of the broad iron  $K_{\alpha}$  iron line does not change significantly on the shortest possible variability timescales which XMM-Newton can probe (Fig. 8), suggesting that the illumination of the disk does not significantly change.

### 4.2 The origin of the narrow iron $K_{\alpha}$ line

One of the main results presented in this paper is that the intensity of the narrow component of the  $K_{\alpha}$  in NGC 5506 remains constant during the whole eight years covered by the XMM-Newton campaign. This extends by a factor of 3 the longest baseline published so far - a  $\sim 1000$  days RXTE monitoring campaign at the end of last century (Lamer et al. 2000). The RXTE/PCA spectroscopic measurements were unable to disentangle the two components (narrow and broad) of the iron  $K_{\alpha}$  line. Nonetheless Lamer et al. (2000) claimed that the strength of the continuum reflection component and the total EW of the iron lines were stronger during phases of low flux. The origin of the iron  $K_{\alpha}$  emission line has challenged the ingenuity of observational and theoretical astronomers since its early discovery (Mushotzky 1982; Turner & Pounds 1989). Evidence that this spectral feature is almost invariably accompanied by a Compton reflection continuum component (Pounds et al. 1990; Nandra & Pounds 1994) in unobscured AGN suggested an origin in optically thick material out of the line of sight. The origin of very broad and skewed profiles in the innermost region of the accretion disk is a matter of heated debate, that we briefly summarised in Sect. 1 (we will further discuss this point in Sect. 4.3). As far as narrower (typical Full Width Half Maximum, FWHM,  $\lesssim 3000$  km  $s^{-1}$ ) and symmetric lines are concerned, possible physical locations for the line-emitting matter are the external regions of the accretion disk (Fabian et al. 1989), the Broad Line Regions (BLRs) (Yaqoob et al. 2001; Bianchi et al. 2008) or the molecular torus (Ghisellini et al. 1994; Krolik et al. 1994). These systems have sizes from a fraction to several tens of parsecs. The lack of correlation between the FWHM of the iron  $K_{\alpha}$  and that of the  $H_{\beta}$  lines (or the black hole mass) disfavors a general origin in the BLRs (Nandra 2006).

We can use the lack of variability of the narrow component of the iron  $K_{\alpha}$  fluorescent line to estimate the dimension of its production region. The line produced by a reflector at distance  $d$  from an illuminating source tracks the variability pattern of the primary continuum if  $d \lesssim t_{var}/c$ , where  $t_{var}$  is the continuum variability timescale and  $c$  is the speed of light. We estimate  $t_{var}$  as the longest time interval between XMM-Newton observations, whose 2–10 keV



absorption-corrected fluxes differ by more than 27%, *i.e.* than the upper limit on the percentage fractional variability of the iron line intensity.  $t_{var}$  hence corresponds to the span between observations XMM1 and XMM8: 7.92 years. This estimate is qualitatively in agreement with the determination of the Power Spectrum Density by the RXTE/PCA monitoring campaign (Uttley & McHardy 2005), which exhibits a slope of  $\simeq -1$  below  $\nu \simeq 4 \times 10^{-5}$  Hz and down to  $\simeq 6 \times 10^{-9}$  Hz. The XMM-Newton results constrain the location of the optically-thick matter responsible for the bulk of the iron  $K_\alpha$  narrow component at a distance  $\gtrsim 2.5$  pc. This is consistent with the best estimate of the inner side of the torus ( $< 5$  pc; Prieto & Meisenheimer 2004). Unfortunately no direct estimate of the Broad Line Region size is available for NGC 5506. The 2–10 keV X-ray luminosity from the data presented in this paper is in the range  $\simeq 6\text{--}11 \times 10^{42}$  erg s $^{-1}$ , which corresponds to a typical size of the BLR  $\lesssim 10$  days (Kaspi et al. 2005). This makes the torus the most likely origin of the narrow iron  $K_\alpha$  line.

We report a possible change in the intensity of the FeXXVI during two of the observations in 2004 performed a few weeks apart, as well as a possible ionisation change of the FeXXV (from a resonance- to a forbidden-dominated state) during XMM8. Given, however, the spectral complexity around 7 keV, a confirmation of these findings through instrumentation with a much better energy resolution is needed. This is shown, for instance, by the different results on the forbidden component of the He-like during XMM8 when one compares the phenomenological (Sect. 3.2) and the relativistic model (Tab. 2).

### 4.3 The origin of the broad iron $K_\alpha$ line

This paper reports the discovery of a broad ( $\sigma \simeq 330$  eV) component of the iron  $K_\alpha$  fluorescent emission line in NGC 5506. The line profile lacks a prominent red wing, in contrast to what typically observed in unobscured Seyfert galaxies (Miller 2007). Although fits with a relativistically broadened profile yield marginally better statistical quality than symmetric Gaussian broadening, it is worth posing the question of whether this difference may be due to a different physical mechanism responsible for the observed broadening.

The symmetric and highly localised profile rules out an explanation in terms of blending of transitions corresponding to different iron ionisation states, enhanced continuum reflection (Guainazzi 2002; Risaliti 2002), scattering from a relativistic wind (Titarchuk et al. 2009) or incorrect fitting of the opacity affecting the underlying continuum (Turner & Miller 2009). Comptonization of line photons was suggested to explain the first observations of broad lines by *Ginga* (Czerny et al. 1991). The observed moderate width requires the line photons to cross at most 3 Compton depths of cool ( $kT_C \leq 0.7$  keV;  $\sigma = \sqrt{2kT/mc^2}$ ) gas (Pozdnyakov et al. 1979; Sunyaev & Titarchuk 1980). The main shortcoming of this scenario, however, is the non-linear dependence of the line EW on the continuum flux on timescales as short as a few hundreds seconds, which is at odds with the line-emitting region being screened by optically thick matter.

The explanation in terms of a relativistically broadened and skewed profile is consistent with the data. For-

mal fits require a moderate inclination ( $i \simeq 40^\circ$ ) accretion disk. NGC 5506 joins the so far restricted club of obscured AGN, which require relativistic effects from a moderately inclined ( $i \simeq 40^\circ$ ) accretion disk, together with MCG-5-23-16 (Balestra et al. 2004) and NGC 526A (Nandra et al. 2007). All the above sources exhibit a column density obscuring the active nucleus in the range  $10^{22\text{--}23}$  cm $^{-2}$ . Although it is tempting to associate these sources with AGN seen through the rim of the obscuring torus (see, for instance, the discussion in Matt et al. 2003), it should be borne in mind that several unobscured AGN in the Nandra et al. (2007) also formally require large inclination angles (*e.g.* Akn 120, Mkn 590, NGC 7213, NGC7469). On the other hand, the recently discovered broad iron lines in IRAS13197-1627 (Dadina & Cappi 2004; Miniutti et al. 2007a) and NGC 1365 (Risaliti et al. 2009) require moderate disk inclinations of  $i \simeq 27^\circ$  and  $24^\circ$ , respectively. A comparison between unbiased samples is needed before any inference on the geometrical configuration of the torus and the disk in X-ray obscured AGN can be drawn from X-ray spectroscopy of the relativistically broadened  $K_\alpha$  line. Moreover, the disk inclination in NGC 5506 is significantly smaller than the inclination of the galaxy disk (Imanishi 2000).

The broad line is not extremely relativistic. It lacks the prominent red wing extending down to  $\simeq 4$  keV observed in, *e.g.*, MCG-6-30-15 (Fabian & Vaughan 2003; Miniutti et al. 2007a), which requires very steep radial emissivity profiles (Wilms et al. 2001). The inner radius of the line emitting region (constrained by the data to be comprised between 3 and 25  $r_g$ ) and the flat emissivity profile suggest that a large area on the disk contributes to the average profile. The line profile is remarkably constant in intensity-resolved spectra, which sample variations of the intrinsic flux on time scales as low as a few hundred seconds (*cf.* Fig. 8) (against at odd with MCG-6-30-15; Iwasawa et al. 1999). The fits do not require statistically significant changes in the structure of the innermost accretion flow. The parameters  $\alpha$  and  $r_{in}$  describing the profile of the relativistically broadened iron line are consistent with being constant over 5 epochs of observations spanning 9 years.

Little is known of the black hole mass in NGC 5506. Both the central stellar velocity dispersion ( $\simeq 180$  km s $^{-1}$ ) (Oliva et al. 1999; Gebhardt et al. 2000; Ferrarese & Merrit 2000; Papadakis 2004) and the width of the [OIII] line (Boroson 2003) suggest a black hole mass  $\sim 10^8 M_\odot$ . For this mass the shortest measured X-ray variability timescale implies that the bulk of high-energy continuum production and reprocessing occur within a few Schwarzschild radii from the black hole. This is in disagreement with the lack of extreme relativistic line broadening, as well as more generally with the idea that NLSy1 Galaxies are characterised by small black hole masses and high accretion rates ( $\lesssim 2\%$  in this scenario) (Komossa 2007). However, X-ray-based estimates suggest that the black hole mass in NGC 5506 could be significantly lower. McHardy et al. (2006) observe that lowering the black hole mass by a factor  $\sim 5$  would bring NGC 5506 to the locus in the PDS break frequency, black hole mass and accretion rate plane shared by AGN and Galactic Black Hole systems. An even more radical revision ( $M_{BH} \simeq 5 \times 10^6 M_\odot$ ) has been proposed by Nikolajuk et al. (2009) on the basis of

the correlation with the X-ray 2–10 keV light curve excess variance. A black hole mass of this order ( $\sim 2 \times 10^6 M_{\odot}$ ) had been proposed by Hayashida et al. (1998) using similar arguments. The light crossing time of the shortest variability timescale if one assumes the Nikolajuk et al. (2009) estimate corresponds to about 20 Schwarzschild radii, in better agreement with broad iron line spectroscopy results. In this case the accretion rate is  $\simeq 40\%$  of the Eddington limit, if one estimates the bolometric luminosity by applying a luminosity-dependent bolometric correction to the 2–10 keV luminosity (Marconi et al. 2004). The size of the BLR,  $r_{BLR} \sim GM/v^2$ , is  $\sim 8$  days, if one estimates  $v$  from the FWHM of the Pa $\beta$  broad component (Nagar et al. 2002).

The size of the AGN sample with robust detections of relativistic lines is still far too small for correlations with other observables to yield stringent constraints. However, it is suggestive that many of the objects of Nandra et al. (2007) “dream team” of relativistic AGN are NLSy1s (Mkn 766, NGC 4051, NGC 5506, NGC 7314) or at least characterised by extreme variability on short (MCG-6-30-15, NGC 4395) or long (NGC 2992) timescales. Possible observational biases are discussed (and ruled out) by Nandra et al. (2007). A trend towards relativistically broadened lines being more common in Narrow Line AGN seems to be present in the stacked spectra of large samples of unobscured AGN (Longinotti et al. 2008). However, there doesn’t seem to be a correlation between the detection of relativistically broadened iron lines and either the accretion rate or the black hole mass in the, *e.g.*, FEROS sample (Longinotti et al. 2008). Once again, the small size and incompleteness of the available samples hamper firm conclusions.

## ACKNOWLEDGEMENTS

Based on observations obtained with XMM-Newton, an ESA science mission with instruments and contributions directly funded by ESA Member States and NASA. Useful discussions with Michal Dovčiak and Giovanni Miniutti are gratefully acknowledged. A careful reading of the manuscript by an anonymous referee significantly improved the presentation of the results.

## REFERENCES

- Anders E. & Grevesse N., 1989, *Geochimica et Cosmochimica Acta* 53, 197
- Antonucci R.R.J., Miller J.S., 1985, *ApJ* 297, 621
- Antonucci R., 1993, *ARA&A* 31, 473
- Balestra I. Bianchi S., Matt G., 2004, *A&A*, 415, 437
- Bennett C.L., et al., 2003, *ApJS*, 148, 1
- Bianchi S., Balestra I., Matt G., Guainazzi M., Perola G.C., 2003, *A&A*, 402, 141
- Bianchi S., La Franca F., Matt G., et al., 2008, *MNRAS*, 389, L52
- Boroson T.A., 2003, *ApJ*, 585, 647
- Czerny B., Zbyszewska M., Raine D.J., 1991, in Treves A. (ed.), *Iron Line Diagnostics in X-ray Sources*, Springer-Verlag, Berlin, p.226
- Dadina M., Cappi M., 2004, *A&A*, 413, 921
- Dewangan G.C., Griffiths R.E., 2005, *ApJ*, 625, L31
- Dovčiak M., Karas V., Yaqoob T., 2004, *ApJS*, 153, 205
- Fabian A.C., Rees M.J., Stella L., White N.E., 1989, *MNRAS*, 238, 729
- Fabian A.C. & Vaughan S., 2003, *MNRAS*, 340, L28
- Ferrarese L., Merrit D., 2000, *ApJ*, 539, L9
- Gabriel C., Denby M., Fyfe D. J., Hoar J., Ibarra A., 2003, in ASP Conf. Ser., Vol. 314 *Astronomical Data Analysis Software and Systems XIII*, eds. F. Ochsenbein, M. Allen, & D. Egret (San Francisco: ASP), 759
- Gebhardt K., Bender R., Bower G., et al., 2000, *ApJ*, 539, L13
- George I.M., Fabian A.C., 1991, *MNRAS*, 249, 352
- Ghisellini G., Haardt F., Matt G., 1994, *MNRAS* 267, 743
- Guainazzi M., 2002, *MNRAS*, 329, L13
- Guainazzi M., Bianchi S., 2007, *MNRAS*, 374, 1290
- Haardt F., Maraschi L., Ghisellini G., 1997, *ApJ*, 476, 620
- Hayashida K., Miyamoto S., Kitamoto S., Negoro H., Inoue H., 1998, *ApJ*, 500, 642
- Kaspi S., Maoz D., Netzer H., Peterson B.M., Vestergaard M., Jannuzi B.T., 2005, *ApJ*, 629, 61
- Komossa S., 2007, *RMxAC*, 32, 86
- Krolik J.H., Madau P., Życki P.T., 1994, *ApJ* 420, L57
- Imanishi M., 2000, *MNRAS*, 313, 1651
- Iwasawa K., Fabian A.C., Young A.J., Inoue H., Matsumoto C., 1999, 306, L19
- McHardy I., Czerny B., 1987, *Nat*, 325, 696
- Lamer G., Uttley P., McHardy I.M., 2000, *MNRAS*, 319, 949
- Longinotti A.L., de la Calle I., Bianchi S., Guainazzi M., Dočiak M., 2008, *RMxAC*, 32, 62
- Magdziarz P. & Zdziarski A.A., 1995, *MNRAS* 273, 837
- Manchanda R.K., 2006, *AdSpR*, 38, 1387
- Marconi A., Risaliti G., Gilli R., Hunt L.K., Maiolino R., Salvati M., 2004, *MNRAS*, 351, 169
- Matt G., 2002, *MNRAS*, 337, 147
- Matt G., Guainazzi M., Maiolino R., 2003, *MNRAS*, 342, 422
- Matt G., Guainazzi M., Perola G.C., Fiore F., Nicastro F., Cappi M., Piro L., 2001, *A&A*, 377, L31
- Matt G., Perola G.C., Piro L., Stella L., 1992, *A&A*, 257, 63 (erratum: 263, 453)
- McHardy I., Koering E., Knigge C., Uttley P., Fender R.P., 2006, *Nat*, 444, 730
- Miniutti G., Fabian A.C., Anabuki N., et al., 2007a, *PASJ*, 59, 315
- Miniutti G., Ponti G., Dadina M., Cappi M., Malaguti G., 2007b, *MNRAS*, 375, 227
- Miller J.M., 2007, *ARA&A*, 45, 441
- Miller L., Turner T.J., Reeves J., 2008, *A&A*, 483, 437
- Molendi S., Bianchi S., Matt G., 2003, *MNRAS*, 343, L1
- Mushotzky R.F., 1982, *ApJ*, 256, 92
- Mushotzky R.F., Fabian A.C., Iwasawa K., Kunieda H., Matsuoka M., Nandra K., Tanaka Y., 1995, *MNRAS*, 272, L9
- Nagar N.M., Oliva E., Marconi A., Maiolino R., 2002, *A&A*, 391, L21
- Nandra K., 2006, 368, L62
- Nandra K., George I.M., Mushotzky R.F., Turner T.J., Yaqoob T., 1997, *ApJ* 467, 70
- Nandra K., O’Neill P.M., George I.M., Reeves J.N., 2007, *MNRAS*, 382, 194
- Nandra K., Pounds K.A., 1994, *MNRAS*, 268, 405
- Nikolajuk M., Czerny B., Gurynowicz P., 2009, *MNRAS*, 394, 2141
- Oliva E., Origlia L., Maiolino R., Moorwood A.F.M., 1999, *A&A*, 350, 9
- Papadakis I.E., 2004, *A&A*, 425, 1133
- Pounds K.A., Nandra K., Stewart G.C., George I.M., Fabian A.C., 1990, *Nat*, 344, 132
- Pozdnyakov L.A., Sobol I.M., Sunyaev R.A., 1979, *A&A*, 75, 214
- Prieto M.A., Meisenheimer K., 2004, *IAUS*, 222, 57
- Reeves J.N., Awaki H., Dewangan G.C., et al., 2007, *PASJ*, 59, 301

- Reeves J.N., Nandra K., George I.M., Pounds K., Turner T.J.,  
Yaqoob T., 2004, ApJ, 602, 648
- Reynolds C.S., Nowak M.A., 2003, PhR, 377, 389
- Risaliti G., 2002, A&A, 386, 379
- Risaliti G., Miniutti G., Elvis M., et al., 2009, ApJ, 696, 160
- Ross R.R., Fabian A.C., 2005, MNRAS, 358, 211
- Strüder L., et al., 2001, A&A 365, L18
- Stuhlinger M., Kirsch M., Santos-LLeó M., et al., 2008,  
“Status of XMM-Newton instrument cross-calibration”  
(ESAC-ESA:Villafranca del Castillo), available at:  
<http://xmm2.esac.esa.int/docs/documents/CAL-TN-0052.ps.gz>
- Sunyaev R.A., Churazov E.M., 1996, Ast.Lett., 22, 649
- Sunyaev R.A., Titarchuk L.G., 1980, A&A, 86, 121
- Tanaka Y., et al., 1995, Nat, 375, 659
- Titarchuk L., Laurent P., Shaposhnikov N., 2009, ApJ, 700, 1831
- Turner M.J.L., et al., 2001, A&A 365, L27
- Turner T.J., Miller L., 2009, A&ARv, 17, 47
- Turner T.J., Pounds K., 1989, MNRAS, 240, 833
- Uttley P., McHardy I.M., 2005, MNRAS, 363, 586
- Yaqoob T., George I.M., Nandra K., et al., 2001, ApJ, 546, 759
- Wang T., Mihara T., Otani C., Matsuoka M., Awaki H., 1999,  
ApJ, 515, 567
- Wilms J., Reynolds C.S., Begelman M.C., Reeves J., Molendi S.,  
Staubert R., Kendziorra E., 2001, MNRAS, 328, L27
- Życki P., Krolik J.H., Zdziarski A.A., Kallman T.R., 1994, ApJ,  
437, 596